NASA Technical Memorandum 78619

Large Eddy Simulation of Turbulent Channel Flow — ILLIAC IV Calculation

John Kim and Parviz Moin

(NASA-TM-78619) LARGE EDDY SIMULATION OF TURBULENT CHANNEL FLOW: ILLIAC 4 CALCULATION (NASA) 21 p HC A02/MF A01 CSCL 02A

N79-32152

Unclas

G3/01 35826

September 1979

National Aeronautics and
Space Administration

NASA Technical Memorandum 78619

Large Eddy Simulation of Turbulent Channel Flow — ILLIAC IV Calculation

John Kim
Parviz Moin, Ames Research Center, Moffett Field, California

NASA
National Aeronautics and
Space Administration

Ames Research Center
Moffett Field, California 94035

LARGE EDDY SIMULATION OF TURBULENT CHANNEL FLOW — ILLIAC IV CALCULATION

John Kim* and Parviz Moin*
Ames Research Center, NASA, Moffett Field, California 94035, U.S.A.

SUMMARY

The three-dimensional time-dependent equations of motion have been numerically integrated for fully-developed turbulent channel flow. The large-scale flow field is obtained directly from the solution of these equations, and the small-scale field motions are simulated through an eddy viscosity model. The calculations are carried out on the ILLIAC IV computer with 64 × 64 × 64 grid points.

The computed flow patterns show that the wall layer consists of coherent structures of low-speed and high-speed streaks alternating in the spanwise direction. These structures were absent in the regions away from the wall. Hot spots, small localized regions of very large turbulent shear stress, are frequently observed. Very close to the wall, these hot spots are associated with $\bar{u}'' > 0$ and $\bar{v} < 0$ (sweep); away from the wall, they are due to $\bar{u}'' < 0$ and $\bar{v} > 0$ (burst). The profiles of the pressure velocity-gradient correlations show a significant transfer of energy from the normal to the spanwise component of turbulent kinetic energy in the immediate neighborhood of the wall ("the splatting effect").

NOMENCLATURE

The overbar ($\bar{\ }$) denotes the filtered component and the prime (') denotes subgrid scale (SGS) component.

C_s — Smagorinsky's constant

$G(\underline{x} - \underline{x}')$ — filter function

h_i — mesh size in the i-direction

h_i^+ — $\equiv \dfrac{h_i u_\tau}{\nu}$

k — wave number $\equiv \sqrt{k_1^2 + k_3^2}$

k_i — wave number in the i-direction

L_x — length of the computational box in the x-direction

L_z — length of the computational box in the z-direction

ℓ — SGS length scale

N — number of mesh points in the y-direction

p — pressure

$\tilde{p}$ — $\equiv \dfrac{\bar{p}}{\rho} + \dfrac{R_{kk}}{3}$

p^* — $\equiv \dfrac{\bar{p}}{\rho} + \dfrac{1}{2}\,\overline{\bar{u}_j\bar{u}_j} + \dfrac{R_{kk}}{3}$

$\hat{p}$ — Fourier transform of $\tilde{p}$

q — root-mean-square velocity

Re — Reynolds number based on channel half-width and the centerline velocity

Re_τ — Reynolds number based on channel half-width and shear velocity

R_{ij} — $\equiv \overline{u_i'u_j'} + \overline{u_j'\bar{u}_i} + \overline{\bar{u}_j u_i'}$

S_{ij} — $\equiv \dfrac{1}{2}\left(\dfrac{\partial \bar{u}_i}{\partial x_j} + \dfrac{\partial \bar{u}_j}{\partial x_i}\right)$ strain rate tensor

t — dimensionless time

u — streamwise velocity

$\bar{u}''$ — $\equiv \bar{u} - \langle\bar{u}\rangle$

u_i — velocity in the i-direction

$\hat{u}_i$ — Fourier transform of $\bar{u}_i$

u_τ — shear velocity $= \sqrt{\tau/\rho}$

v — velocity in the vertical direction

w — velocity in the spanwise direction

x, x_1 — streamwise coordinate

x_i — coordinate in the i-direction

$\underline{x}, \underline{x}'$ — coordinate vector

y, x_2 — coordinate in the direction normal to the walls

y_w — distance to the nearest wall

y^+ — $\dfrac{y_w u_\tau}{\nu}$

z, x_3 — spanwise coordinate

ϵ_{ijk} — the completely antisymmetric tensor of rank 3

λ — mean streak spacing

λ_i — mean spacing of the turbulent structures in the i-direction

λ_i^+ — $\equiv \dfrac{\lambda_i u_\tau}{\nu}$

λ^+ — $\equiv \dfrac{\lambda u_\tau}{\nu}$

ξ_j — jth meshpoint in the vertical direction of the transformed (uniform mesh) space

ρ — density

τ_{ij} — $R_{ij} - \dfrac{R_{kk}\delta_{ij}}{3}$

τ_w — mean wall shear stress

Δt — dimensionless time step

*NRC Research Associate

ν	kinematic viscosity	< >	horizontal average (x-z plane)
ν_T	eddy viscosity	$< >^t$	time average
ω_i	vorticity in the i-direction	**Subscripts**	
ω_x	vorticity in the x-direction	w	wall value
δ_{ij}	$\equiv \begin{cases} 1 & i=j \\ 0 & i \neq j \end{cases}$	SGS	subgrid scale
		Superscript	
		n	time step

1. INTRODUCTION

The technique of large eddy simulation (LES) is a relatively new method for computing turbulent flows. The primary motivation for its undertaking is that the large eddy turbulence structures are clearly flow-dependent (e.g., jets vs boundary layers) and hence they are difficult if not impossible to model. On the other hand, there is experimental evidence (e.g., Ref. 1) that small eddies are universal in character, and consequently much more amenable to general modeling.

In LES, the large-scale motions are computed directly using three-dimensional time-dependent computation, and the small-scale motions are modeled. The dynamical equations for the large-scale field are derived by averaging the Navier-Stokes equations over volumes in space that are small compared to the overall dimensions of the flow field. This averaging is to provide sufficient smoothing of the flow variables, so they can be represented on a relatively coarse mesh. The resulting equations for the large eddies contain terms that involve small-scale turbulence. These terms are replaced by models that are to represent the interaction between the resolved and unresolved (subgrid scale, SGS) field motions.

One of the most extensive applications of LES has been to the problem of decay of homogeneous isotropic turbulence (see Refs. 2-4). A variety of numerical methods and subgrid-scale turbulence models was incorporated to compute this flow. Both the pressure-velocity and the vorticity-stream function formulations of the dynamical equations were used. These studies have shown that homogeneous turbulent flows can be reasonably simulated using simple eddy-viscosity models.

The first application of LES was made by Deardorff (Ref. 5), who simulated a fully developed turbulent channel flow at a very large Reynolds number. Utilizing a modest number of grid points (6,720), he showed that three-dimensional numerical simulation of turbulence (at least for simple flows) is feasible. His calculations predicted some of the features of turbulent channel flow with reasonable success and demonstrated the potential of LES for prediction and analysis of turbulent flows.

Schumann (Ref. 6) has also performed numerical simulation of turbulent channel flow. In addition, he has applied LES to cylindrical geometries (annuli). He used up to 10 times more grid points than Deardorff and a much more complex subgrid-scale model. In that model, an additional equation for SGS turbulent kinetic energy was integrated. However, the results showed no significant improvement over the case in which eddy-viscosity models were used (Ref. 6).

In the calculations of channel flow described above, no attempt was made to compute the flow in the vicinity of the walls. A great portion of turbulent kinetic energy production takes place in this region (see Ref. 7). Therefore, by using artificial velocity boundary conditions well beyond the viscous sublayer and buffer layer, a significant fraction of the dynamics of turbulence in the entire flow was effectively modeled. In addition, it should be noted that the boundary conditions used in the latter calculations assume that in the log layer, the velocity fluctuations are in phase with the wall shear stress fluctuations. This assumption is not supported by experimental measurements (Ref. 8).

Moin et al. (Ref. 9) simulated the channel flow, including the viscous region near the wall. The exact no-slip boundary conditions were used at the walls. In their computations, only 16 uniformly spaced grid points were used in each of the streamwise (x) and spanwise (z) directions and 65 nonuniformly spaced mesh points were used in the y-direction. The grid resolution was especially inadequate in the z-direction to resolve the now well-known streaky structures in the vicinity of the wall. In spite of this, computations did display some of the well-established features of the wall region. In particular, the results showed coherent structures of low-speed and high-speed fluid alternating in the viscous region near the wall, though not at their proper scale. The overall agreement of the computed mean-velocity profile and turbulent statistics with experimental data was satisfactory.

Encouraged by the results of the above coarse calculation, the present numerical simulation of channel flow with 262,144 grid points (64 × 64 × 64) was undertaken. The ILLIAC IV computer, a parallel processor, was chosen for this purpose. Although the grid resolution in the spanwise direction is still not sufficient for an adequate representation of the wall-layer streaks, it is a significant improvement over the earlier calculation. This, in turn, allows a more realistic and comprehensive study of the structure and mechanics of this flow.

This paper is the result of a work that is now in progress and is essentially intended to demonstrate some of the capabilities of LES in the prediction and analyses of wall-bounded turbulent shear flows. In Sec. 2, the dynamical equations for large-scale field motions are derived. The subgrid model that was used is described in Sec. 3; Section 4 describes the computational grid network and its relation to the observed physical length scales in the flow. The numerical method is briefly outlined in Sec. 5; the data management process is taken up in Sec. 6; and in Sec. 7, we examine some aspects of the mechanics and structure of the flow, both in the vicinity of the wall and in regions away from the wall, and an attempt is made to correlate numerical results with laboratory observations. In Sec. 8, we present the computed flow statistics, which include the mean-velocity profile, turbulent intensities, and turbulence shear stress. In that section, we will point out some of the deficiencies of the subgrid-scale model used and suggest improvements. Finally, conclusions are presented in Sec. 9.

2. GOVERNING EQUATIONS FOR THE LARGE-SCALE FIELD

The first step in LES is the definition of the large-scale field. Each flow variable f is decomposed as follows:

$$f = \bar{f} + f' \tag{1}$$

Here, the overbar denotes the large-scale or "filtered" field and the prime indicates the residual or "subgrid" field. Following Leonard (Ref. 10) we define the large-scale field as:

$$\bar{f}(x) = \int_D G(\underline{x},\underline{x}')f(\underline{x}')dx' \tag{2}$$

where G is the filter function and the integral is extended over the whole flow field. In the horizontal planes (x-z), several possible choices for the filter function are available. Unless otherwise stated, most of the calculations reported here were carried out using a Gaussian filter, $G(x-x',z-z')$. The width of the Gaussian function characterizes the smallest scales of motion retained in the filtered field (the largest scales in the residual field). We assume that the filtering in the planes parallel to the walls provides sufficient smoothing in the vertical directions as well; our computations support this assumption. In addition, it should be noted that we use second-order finite difference schemes to approximate partial derivatives in the x_2-direction and such schemes have an implicit filtering effect associated with them. For further details see Moin et al. (Ref. 9).

After applying the filtering operation (Eq. (2)) to the incompressible Navier-Stokes and the continuity equations, the governing equations for the filtered field may be written

$$\frac{\partial \bar{u}_i}{\partial t} - \epsilon_{ijk}\,\overline{\bar{u}_j\bar{\omega}_k} = -\frac{\partial p^*}{\partial x_i} + \delta_{i1} - \frac{\partial}{\partial x_j}\tau_{ij} + \frac{1}{Re_\tau}\frac{\partial^2 \bar{u}_i}{\partial x_j \partial x_j} \tag{3}$$

$$\frac{\partial \bar{u}_i}{\partial x_i} = 0 \tag{4}$$

where we have decomposed u_i as in (1) and

$$\bar{\omega}_k = \epsilon_{pqk}\frac{\partial \bar{u}_q}{\partial x_p}$$

$$\tau_{ij} = R_{ij} - \frac{R_{kk}\delta_{ij}}{3}$$

$$R_{ij} = \overline{u_i'u_j'} + \overline{u_j'\bar{u}_i} + \overline{\bar{u}_j u_i'}$$

$$p^* = \frac{\bar{p}}{\rho} + \frac{1}{2}\overline{\bar{u}_j\bar{u}_j} + \frac{R_{kk}}{3} = \tilde{p} + \frac{1}{2}\overline{\bar{u}_j\bar{u}_j}$$

Here, the variables are nondimensional using the channel half-width δ and the shear velocity $u_\tau = \sqrt{\tau_w/\rho}$. The calculations will be carried out for a fixed streamwise mean-pressure gradient which is accounted for by the δ_{i1} term in the momentum Eq. (3).

3. RESIDUAL STRESS MODEL

The remaining unknown quantity in Eq. (3) is τ_{ij}. This term represents the subgrid-scale stresses and must be modeled. In the present calculations we have used an eddy viscosity model,

$$\tau_{ij} = -2\nu_T S_{ij} \tag{5a}$$

where

$$S_{ij} = \frac{1}{2}\left(\frac{\partial \bar{u}_i}{\partial x_j} + \frac{\partial \bar{u}_j}{\partial x_i}\right) \tag{5b}$$

The small-scale eddy viscosity ν_T represents the action of the unresolved scales of motion on the resolved scales. Hence, as the resolution gets better, ν_T should get smaller. This suggests that ν_T should scale on a length scale ℓ which is directly related to the computational resolution. The model most commonly used for ν_T and the one we use here is the Smagorinsky model,

$$\nu_T = (C_s \ell)^2\sqrt{S_{ij}S_{ij}} \tag{6}$$

where $C_s = 0.1$ (Ref. 5) is a dimensionless constant and ℓ is a dimensionless representative of the grid resolution, here assumed to be (Ref. 5):

$$\ell = (h_1 \cdot h_2(y) \cdot h_3)^{1/3} \tag{7}$$

This expression for ℓ is probably appropriate only for cases in which there is no significant grid anisotropy (Ref. 6). In the present calculation, the computational grid is very elongated ($h_1, h_3 >> h_2$) in the vicinity of the walls, and hence use of Eq. (7) is not strictly justified. However, to gain a better insight into the role of ℓ and to help guide its selection in future calculations, we have used Eq. (7) with a modification described below.

Near the walls, the subgrid-scale turbulence Reynolds number, defined as

$$R_{SGS} = \frac{q_{SGS} \cdot \ell}{\nu} \tag{8}$$

is very small, and hence one expects the value of the eddy viscosity coefficient to be very small. In our calculations, we have found that the damping provided by the presence of $(h_2(y))^{1/3}$ in Eq. (7) is not sufficient, and excessively large subgrid-scale stresses are formed near the wall. Therefore, in the present calculations we have multiplied ℓ (Eq. (7)) by an exponential damping function $1 - \exp(-y^+/50)$.

The eddy-viscosity model used here is best rationalized for isotropic turbulence at the scale of the computational grid. The fundamental assumption behind this model is that the resolution scale lies within an inertial range with the -5/3 power spectrum (Ref. 11). It is clear that for the moderate Reynolds number (Re_τ = 640) that we are considering and the nature of the grid volumes used, the above assumptions are not satisfied. This is particularly true in the highly viscous region in the vicinity of the walls. Thus, the present simulation is viewed as a challenge to the eddy-viscosity model used.

A critical test for the large eddy simulation technique is the prediction of the logarithmic layer and the von Karman "constant." This is one of the reasons for not utilizing the mixing-length model in the present calculations to account for inhomogeneity due to the mean shear (Ref. 6). Such a model is known to "postdict" the correct mean-velocity profile.

4. THE COMPUTATIONAL GRID

The availability of computer resources restricts the size of calculations possible. For a given number of grid points N, we have to choose the grid size(s) based on the known physical properties of turbulent channel flow under consideration.

In the vertical direction ($-1 \leq y \leq 1$), a nonuniform grid spacing is used. The following transformation gives the location of grid points in the vertical direction (Ref. 9):

$$y_j = \frac{1}{a} \tanh [\xi_j \tanh^{-1}(a)] \tag{9}$$

where

$$\xi_j = 1 + 2(j - 1)/(N - 2) \tag{10}$$

$$j = 1, 2, \ldots, N$$

N is the total number of grid points in the y direction, and the adjustable parameter of transformation is a ($0 < a < 1$). We used $a = 0.98346$, $N = 64$. This value of a was selected so that the above grid distribution in the y-direction is sufficient to resolve the viscous sublayer ($y^+ < 5$).

The length L_x and L_z of the computational box in the streamwise (x) and spanwise (z) direction, in which periodic boundary conditions are used, should be long enough to include the important large eddies (Refs. 6, 12). Based on the two-point correlation measurements of Comte-Bellot (Ref. 13), we used $L_x = 2\pi$, and $L_z = 4\pi/3$. We have used 64 uniformly spaced grid points in each of the streamwise and spanwise directions. With the above choices for L_x and L_z, the nondimensional grid spacings in the horizontal directions expressed in the wall units are:

$$h_1^+ = 63$$

$$h_3^+ = 42$$

In the wall region, the important large eddies are the "streaks" (Ref. 14). These have a mean spanwise spacing corresponding to $\lambda_3^+ \approx 100$. It is clear that our grid resolution in the spanwise direction is not quite sufficient to resolve the streaks. This is especially true when we note that the above value for λ_3^+ is based on an ensemble of measurements, and at a given instant streaks with a finer spacing than λ_3^+ can be formed. As we shall see, however, calculations did reveal these structures, though not at their proper scale.

With relatively minor modifications to the present computer program, we are able to perform calculations with 64 × 64 × 128 grid points in the x, y, and z directions, respectively. It is expected that in this simulation the spacing of the wall-layer streaks will be more in line with the laboratory observations.

5. NUMERICAL METHOD

A complete description of the numerical method used is given in Ref. 15. Here, we give a brief outline of the method and minor modifications that were made to enhance the data management process. The partial derivatives in the x_2 direction were approximated by second-order central difference formulae. In the x_1 and x_3 directions, partial derivatives were evaluated pseudospectrally (Ref. 16). With a given number of grid points, the use of the pseudospectral method in any given direction gives us the best possible resolution in that direction. This is particularly useful in the x_3 direction where we face a lack of grid resolution (Sec. 4).

Time advancement is made using a semi-implicit method. Pressure, viscous terms, and part of the subgrid-scale model are treated implicitly, whereas explicit time advancement is used for the remaining nonlinear terms. The equation of continuity is solved directly. Second-order Adams Bashforth (Ref. 17) and Crank-Nicolson (Ref. 18) methods are used for explicit and implicit time advancement, respectively.

Next, we Fourier transform the resulting equations in x_1 and x_3 directions. This converts the above set of partial differential equations to the following set of ordinary differential equations for the variables at time step $n + 1$, for every pair of Fourier wave numbers k_1 and k_3, with $y = x_2$ as the independent variable.

$$\frac{\partial^2 \hat{u}_1^{n+1}}{\partial y^2} + (\beta_1 - k^2)\hat{u}_1^{n+1} + ik_1\beta_1 \frac{\Delta t}{2} \hat{p}^{n+1} = \hat{Q}_1{}^n \tag{11a}$$

$$\frac{\partial^2 \hat{u}_2^{n+1}}{\partial y^2} + (\beta_2 - k^2)\hat{u}_2^{n+1} + \beta_2 \frac{\Delta t}{2} \frac{\partial \hat{p}^{n+1}}{\partial y} = \hat{Q}_2{}^n \tag{11b}$$

$$\frac{\partial^2 \hat{u}_3^{n+1}}{\partial y^2} + (\beta_3 - k^2)\hat{u}_3^{n+1} + ik_3\beta_3 \frac{\Delta t}{2} \hat{p}^{n+1} = \hat{Q}_3{}^n \tag{11c}$$

$$ik_1\hat{u}_1^{n+1} + \frac{\partial \hat{u}_2{}^{n+1}}{\partial y} + ik_3\hat{u}_3^{n+1} = 0 \tag{11d}$$

Here, β_i $(i = 1,2,3)$ are known functions of Re_τ and $\langle\nu_T{}^n\rangle$, and $\hat{Q}_i{}^n$ represent the terms involving the velocity and pressure field at time-step n and $n - 1$ (see Ref. 15).

In addition to the use of implicit time advancement for all the viscous terms, the algorithm used in the present study is different in one other respect from the one described in Ref. 15. For reasons that will be explained in the next section, Eqs. (11a) and (11c) were multiplied by ik_1 and ik_3, respectively. Thus, the dependent variables for the time-advancement equations are $ik_1\hat{u}$, $\hat{v}$, and $ik_3\hat{w}$ rather than $\hat{u}$, $\hat{v}$, and $\hat{w}$.

The remaining steps in the solution procedure are as follows. Finite difference operators (described above) are used to approximate $\partial/\partial y$ and $\partial^2/\partial y^2$. This gives a set of linear algebraic equations for the Fourier transform of dependent variables. This system is of block tridiagonal form and can be solved very efficiently. No-slip boundary conditions are used at the solid boundaries. Finally, inversion of the Fourier transform gives the velocity and pressure field at time-step $n + 1$.

The initial velocity field was the same as the one used in Ref. 9 interpolated on the finer grid used here.

6. DATA MANAGEMENT

In large simulations, the high-speed random-access memory of the computer on hand may not hold the entire data base of the problem being considered. In the present case, the core memory of the ILLIAC IV is large enough to hold only a few planes of velocity pressure field. Therefore, it is essential to manage the flow of data efficiently between the core memory and the disk memory where the entire data base resides. In general, separate passes over the data base are required for each time step and the task is to minimize the required number of such passes. The following describes a data management process employed in the present simulation.

The system of Eq. (11) must be solved for both real and imaginary parts of the dependent variables. This necessarily means that two passes through the data base are required: one for real parts of $\hat{u}_1$ and $\hat{u}_3$ and imaginary parts of $\hat{u}_2$ and $\hat{p}$, and the other for imaginary parts of $\hat{u}_1$ and $\hat{u}_3$ and real parts of $\hat{u}_2$ and $\hat{p}$.

To avoid an extra pass through the data base, we multiply Eqs. (11a) and (11c) by ik_1 and ik_3, respectively (Ref. 19). (These multiplications in Fourier space amount to differentiations in real space.)

$$\frac{\partial^2 \tilde{u}_1^{n+1}}{\partial y^2} + (\beta_1 - k^2)\tilde{u}_1^{n+1} - k_1{}^2\beta_1 \frac{\Delta t}{2} \hat{p}^{n+1} = \tilde{Q}_1{}^n \tag{12a}$$

$$\frac{\partial^2 \tilde{u}_2^{n+1}}{\partial y^2} + (\beta_2 - k^2)\tilde{u}_2^{n+1} + \beta_2 \frac{\Delta t}{2} \frac{\partial \hat{p}^{n+1}}{\partial y} = \tilde{Q}_2{}^n \tag{12b}$$

$$\frac{\partial^2 \tilde{u}_3^{n+1}}{\partial y^2} + (\beta_3 - k^2)\tilde{u}_3^{n+1} - k_3{}^2\beta_3 \frac{\Delta t}{2} \hat{p}^{n+1} = \tilde{Q}_3{}^n \tag{12c}$$

$$\tilde{u}_1^{n+1} + \frac{\partial \tilde{u}_2^{n+1}}{\partial y} + \tilde{u}_3^{n+1} = 0 \tag{12d}$$

where $\tilde{u}_1 = ik_1\hat{u}_1$; $\tilde{u}_2 = \hat{u}_2$; $\tilde{u}_3 = ik_3\hat{u}_3$; $\tilde{Q}_1{}^n = ik_1\hat{Q}_1{}^n$; $\tilde{Q}_2{}^n = \hat{Q}_2{}^n$; and $\tilde{Q}_3{}^n = ik_3\hat{Q}_3{}^n$. The above system of equations can be solved with one pass through the data base, but two extra integrations in the Fourier space are required to obtain u_1 and u_3 in physical space. It should be noted, however, that such integrations cost far less than an I/O pass. In addition, to avoid the loss of information, upon differentiation, the Fourier mode associated with a null wave number is simply not multiplied by its wave number (i.e., zero) and, similarly, it is not divided by its wave number upon integration. This implies that $\bar{u}_1$, $\bar{u}_2$, and $\bar{u}_3$ in Eqs. 12 should be understood as

$$\hat{u}_1(0,y,k_3);\; ik_1\hat{u}_1(k_1,y,k_3), k_1 \neq 0$$

$$\hat{u}_2(k_1,y,k_3)$$

$$\hat{u}_3(k_1,y,0);\; ik_3\hat{u}_3(k_1,y,k_3), k_3 \neq 0$$

The system of Eqs. (12) is solved by two separate passes through the data base. In PASS 1, the right-hand sides of these equations, Q_i $(i = 1,2,3)$, are evaluated and in PASS 2, the block tridiagonal system is solved. To compute the right-hand side vector in PASS 1, differentiations in all spatial directions are required. Since the pseudospectral method is used in the horizontal directions (x and z) and a finite-difference scheme is used in the normal direction (central difference), all the data in an (x - z) plane are needed for operators in these directions and the data for at least three adjacent planes are needed for finite difference operators in the y direction. Therefore, in PASS 1, two (x - z) planes are brought into the core to be handled by a double buffer scheme. One complete pass through the data base is required to complete PASS 1.

In PASS 2, the block tridiagonal system must be solved for each k_1 and k_3. In this pass, two $(y - k_3)$ planes are brought into the core. A special algorithm had to be developed to solve the block tridiagonal matrix because of the limitation on the core size. In a conventional-block tridiagonal solver, all the results of forward sweep are stored to be used in backward sweep. For the present simulation, this would require half of the total core size (i.e., 16 × 64 × 64) which is not feasible. Hence, a special algorithm* was developed so that only a part of the results of the forward sweep is stored in the memory and the rest is recomputed as necessary in the backward sweep. Although this requires extra computations in the backward sweep, this method is much more efficient than performing the extra I/O passes that would otherwise have been necessary.

The computation described here was carried out on the ILLIAC IV computer at Ames Research Center. The dimensionless time step, during most of the calculations, was set at $\Delta t = 0.001$. The computer time per time-step (CPU and I/O time) was about 22 sec. This computational speed has been achieved with a full use of the parallel processing capabilities of the ILLIAC IV and the data management process just described.

7. DETAILED FLOW STRUCTURES

In this section, we investigate the detailed flow patterns by examining contour plots of typical instantaneous velocity and vorticity fields in x-z, x-y, and y-z planes. In all these plots positive values are contoured by solid lines and negative values are contoured by dashed lines. In addition, all the plots are obtained at a given dimensionless time (t = 1.4).

Figure 1 shows patterns of $\bar{u}''$ in an x-z plane very close to the lower wall ($y^+ = 16.1$). The striking feature of this figure is the existence of highly elongated (in the x-direction) regions of high-speed fluid located adjacent to low-speed ones. This picture of the flow pattern in the vicinity of the wall is in agreement with experimental observations (Refs. 20, 21) that the wall layer consists of relatively coherent structures of low-speed and high-speed streaks alternating in the spanwise direction. Examination of the typical spanwise spacing of these structures shows significant improvement over the earlier simulation (Ref. 9) where only 16 uniform grid points were used in each of the spanwise and streamwise directions. However, the typical spacing of these streaks is still about 3 times larger than the experimentally observed mean value of $\lambda_3^+ \approx 100$. This is expected, since our computational grid size in the spanwise direction is too large to resolve the wall layer streaks in their proper scale (Sec. 4).

Figure 2 shows patterns of $\bar{u}''$ in an x-z plane far away from the wall ($y/\delta = 0.73$). It is clear that the $\bar{u}''$ patterns in the regions away from the wall do not show the coherent streaky structures that are characteristic of wall-layer turbulence. This is also in agreement with the experimental observations (Ref. 20). In fact, it is difficult to associate a definite structural pattern to $\bar{u}''$ in the regions away from the wall.

Since turbulent energy production is directly proportional to $-\langle uv\rangle^t$, it is important to study the instantaneous map of $\bar{u}''\bar{v}$. Figure 3 shows the patterns of $\bar{u}''\bar{v}$ in the same x-z plane as in Fig. 1; that is, very close to the wall ($y^+ = 16.1$). Examination of this figure reveals several points related to the dynamics of wall-layer turbulence that deserve attention. First, it can be seen that the regions with negative $\bar{u}''\bar{v}$, which have a positive contribution to the production of average turbulent kinetic energy, constitute the overwhelming majority of the entire plane. Second, pronounced streamwise elongation, the characteristic of the wall layer $\bar{u}''$ eddies, is absent in $\bar{u}''\bar{v}$ patterns. This indicates that in contrast to $\bar{u}''$ eddies, $\bar{v}$ eddies are not significantly elongated in the x-direction. Third, there are several small regions (hot spots), that are associated with very large values (large concentrations of dashed lines) of $-\bar{u}''\bar{v}$. These regions are highly localized in space. Overlaying Fig. 3 on Fig. 1 reveals that the great majority of the "hot spots" are associated with $\bar{u}'' > 0$ (hence, $\bar{v} < 0$). Thus, it appears that in the close vicinity of the wall most of the regions with very large values of $(-\bar{u}''\bar{v})$ are associated with high-speed fluid approaching the wall (sweeps) rather than low-speed fluid being ejected from the wall (bursts). With combined visual and hot-wire measurements, Falco (Ref. 22) has identified a new flow module in the vicinity of the wall. These relatively small but energetic structures (called pockets) appear to be footprints of high-speed fluid moving toward the wall. It is possible that the hot spots identified here may be related

*The original concept was suggested to us by Marshall Merriam, Ames Research Center.

to pockets. Figure 4 shows the contour plots of $\tilde{u}''\tilde{v}$ in the x-z plane located at $y^+ = 90$. Examination of this figure and the corresponding $\tilde{u}''$ plot (not shown here) shows that in contrast to the near-wall region most of the hot spots that can be identified in this plane are associated with $\tilde{u}'' < 0$ and $\tilde{v} > 0$, that is, with bursts. With quadrant analysis of uv, Brodkey et al. (Ref. 23) have found that most of the contribution to $-\langle uv \rangle^t$ in the wall region comes from sweeps, and that in the regions away from the wall it comes from ejections. This is consistent with what is observed here in relation to Figs. 3 and 4. There are two other features in Fig. 4 that deserve attention. First, similar to Fig. 1, the regions with negative $\tilde{u}''\tilde{v}$ constitute the overwhelming majority of the entire plane. Although there are regions with very large positive $\tilde{u}''\tilde{v}$, they are highly localized in space. Second, the maximum value of $(-\tilde{u}''\tilde{v})$ in this plane is 17.81. This is about 20 times the expected $\langle -uv \rangle^t$ at this plane. Such large excursions of $\tilde{u}''\tilde{v}$ from its expected mean value have been a frequent observation in the laboratory (e.g., see Ref. 24).

Figure 5 shows contour plots of $\tilde{u}''\tilde{v}$ in an x-z plane far away from the lower wall ($y/\delta = 0.73$). In contrast to planes located close to the lower wall (Figs. 3, 4), where the regions with negative $\tilde{u}''\tilde{v}$ dominated the entire planes, a significant portion of this plane is associated with large positive $\tilde{u}''\tilde{v}$ as well as negative $\tilde{u}''\tilde{v}$. The regions with the largest positive $\tilde{u}''\tilde{v}$ are associated with high-speed fluid moving toward the upper wall, and the regions with the largest $-\tilde{u}''\tilde{v}$ seem to be evenly distributed among high-speed fluid moving toward the lower wall or low-speed fluid moving away from the lower wall. Finally, examination of the $\tilde{u}''\tilde{v}$ patterns in the midplane (not shown here) reveals that in contrast to the plane just described ($y/\delta = 0.73$), the regions with the largest $\tilde{u}''\tilde{v}$ are associated with bursts originating in the upper half of the channel, whereas the regions with the largest $-\tilde{u}''\tilde{v}$ correspond to bursts originating in the lower half of the channel.

Among the conceptual models of the inner region of turbulent boundary layers is the streamwise vorticity model. This model portrays the inner region as being composed of pairs of long counter-rotating streamwise vortices located adjacent to each other. These long vortical structures, in turn, create low-speed and high-speed streaks alternating in the spanwise direction. Figure 6 shows the streamwise vorticity patterns in the same x-z plane as in Fig. 1 ($y^+ = 16$). These patterns do not show elongated regions of positive and negative $\tilde{\omega}_x$ alternating in the spanwise direction. Moreover, no definite relationship appears to exist between the streak patterns shown in Fig. 1 and $\tilde{\omega}_x$ patterns shown in Fig. 6. Therefore, the present simulation tends to dispute the validity of the vorticity model.

Figures 7 and 8 show patterns of $\tilde{u}''$ and $\tilde{\omega}_z$ in an x-y plane, $z = 15h_3$. For clarity, we have expanded the region $0 \leq y/\delta \leq 0.5$. A pronounced feature of Fig. 7 is the two regions of high-speed fluid (with respect to the local mean velocity) that are inclined at oblique angles with respect to the wall. These structures are apparently associated with intense shear layers that are also inclined with respect to the wall (Fig. 8). Similar large-scale structures have also been observed in the laboratory. From measurements of space-time correlation of wall shear stress and velocity fluctuations in a turbulent duct flow, Rajagopalon and Antonia (Ref. 8) have identified large-scale structures that are inclined at a mean angle of about 13° to the wall. At this time, we have not scanned a sufficient number of x-y planes at widely spaced times to obtain the mean inclination angle of these structures.

In Figs. 9 through 14, contour plots of the velocities and the streamwise vorticity in a y-z plane ($x = 0$) are shown. The contour plots in this plane reveal the existence of surprisingly well-organized structures in the wall region. Figure 9 shows a contour plot of the streamwise velocity $\tilde{u}''$. Note that the figure is stretched 4 times in the vertical direction and that the contour line patterns are thus distorted in that direction. Two important features can be observed in this figure. First, away from the wall – for example, $y/\delta > 0.4$ – no definite structure is discernible. Near the wall, however, an alternating array of low-speed and high-speed fluid is noticeable. This array has a long streaky structure in the streamwise direction, as was shown in Fig. 1. Second, as we approach the wall, the size of the eddies decrease, gradually. Figure 10 is a magnified version of Fig. 9 close to the wall, $0 < y^+ < 46$. Again, the figure is highly stretched in the y direction so that the shapes of the flow structures are distorted. The array of low-speed and high-speed fluid is clearly discernible in this figure. This strikingly well-organized flow structure in the wall region is consistent with the previous experimental observations (Ref. 20), although the typical spacing between the streaks is not correct because of the insufficient spanwise grid spacings mentioned earlier. In addition to the well-organized structure in the wall region, there exists a very intense shear layer in the vertical plane where the low-speed and high-speed fluids come close together. This could cause free-shear-layer-type instabilities in this plane; such instabilities might be related to the experimental observations that the lifted streaks oscillate not only in the vertical direction but also in the horizontal planes.

Figure 11 shows a contour plot of the normal velocity $\tilde{v}$ in the same plane as in Fig. 10. Here, a positive $\tilde{v}$ (the solid lines) represents fluid moving away from the wall, and a negative $\tilde{v}$ (the dashed lines) represents fluid moving toward the wall. In this figure we notice an array of fluid moving away and toward the wall. If we align Fig. 10 with Fig. 11, we notice that, generally, there exists a negative correlation between $\tilde{u}''$ and $\tilde{v}$. Note that in the vicinity of the wall, the low-speed fluid elements ($\tilde{u}'' < 0$) are generally being ejected away from the wall ($\tilde{v} > 0$), while high-speed fluid elements are moving toward the wall. Clearly, the fluid motions just described have a positive contribution to the production of averaged turbulent kinetic energy.

Figure 12 shows a contour plot of the spanwise velocity $\tilde{w}$. A positive $\tilde{w}$ (solid lines) represents fluid moving to the right and a negative $\tilde{w}$ (dashed line) represents fluid moving to the left. Note also that a significantly large spanwise velocity gradient in y – that is, $\partial\tilde{w}/\partial y$ – exists due to the no-slip boundary conditions at the wall. This results in substantial streamwise vorticity near the wall, although flow is not actually revolving in this region. We will come back to this later. If we now align the contour plot of $\tilde{w}$ with that of $\tilde{v}$, we can identify a definite flow pattern that exists in the wall region. A schematic illustration of this flow pattern is given in Fig. 15. This simplified illustration shows how low-speed streaks are being formed and lifted away from the wall. It is interesting to note that the rotation of the streamwise vorticity is in the opposite direction to the conventional vorticity model (Ref. 25) (see also Fig. 15b).

Figure 13 shows a contour plot of $\bar{\omega}_x$ in the y-z plane at x = 0. It can be seen that $\bar{\omega}_x$ is concentrated only in the wall region. Away from the wall, the strength of the vorticity becomes very weak and no organized structure is discernible. Near the wall, highly localized concentrations of $\bar{\omega}_x$ appear, sometimes in pairs of opposite sign. Figure 14 is a close-up of the wall region for $y^+ \leq 46$. Again, the figure is highly stretched in the vertical direction so that the patterns are distorted. By comparing these contour plots with those of $\bar{v}$ and $\bar{w}$, we can distinguish the streamwise vorticity associated with the revolving fluid motion from the one associated with the velocity gradients. Recall that the existence of $\bar{\omega}_x$ does not guarantee large-scale revolving fluid motion. In fact, most $\bar{\omega}_x$ very close to the wall, say $y^+ < 10$, is due to $\partial\bar{w}/\partial y$ and is not related to the revolving motion. Some of $\bar{\omega}_x$ away from the wall, however, (e.g., the one in the center in Fig. 14) is associated with a large-scale revolving motion. This is in agreement with the experimental observations by flow visualization techniques (Ref. 7) where strong revolving motions are observed away from the wall ($y^+ > 10$) and not very close to it. It should also be noted that although the strong vortical revolving fluid motion appears outside the sublayer, in the present simulation, the root-mean-square value of $\bar{\omega}_x$, $\langle\bar{\omega}_x^2\rangle^{1/2}$ always attains its maximum at the wall [note that $\bar{\omega}_x|_{wall} = (\partial\bar{w}/\partial y)|_{wall}$].

8. MEAN VELOCITY PROFILE AND TURBULENCE STATISTICS

Figure 16 shows the mean-velocity profile $\langle\bar{u}\rangle$ that has developed after two dimensionless time units. (One nondimensional time unit corresponds approximately to the time in which a particle moving with centerline velocity travels 22δ.) Note that in the present study horizontal-average values are approximately ergodic. The calculated velocity profile shows a distinct logarithmic region over an appreciable portion of the channel width. For comparison, we have also included some of the available experimental data in this figure. The agreement of the computed mean-velocity profile with experimental data in most of the channel is satisfactory. In the vicinity of the wall, however, the values of the computed mean-velocity profile are rather low. This is due to the presence of an excessively large eddy viscosity coefficient near the wall. To verify this observation, we carried out a set of calculations (starting from t = 1.0) where instead of the eddy viscosity model, we used a subgrid scale model similar to the one used by Fornberg (Ref. 26; in our numerical experiment, small-scale turbulence is removed by a sharp cut-off filter at each time step). Although this model is rather inadequate for proper representation of the interaction between the subgrid-scale and resolvable scale motions, it suffices for our present purpose, especially if the total time of integration is not large. Figure 17 shows the resulting $\langle\bar{u}\rangle$ profile at t = 1.5. It is clear that the profile of $\langle\bar{u}\rangle$ has attained the proper values in the vicinity of the wall. In addition, the logarithmic layer is once again evident. Figure 18 shows the profiles of resolvable normal turbulent intensities, $\langle\bar{u}''^2\rangle^{1/2}$, $\langle\bar{v}^2\rangle^{1/2}$, and $\langle\bar{w}^2\rangle^{1/2}$ at the same time as in Fig. 16. It can be seen that in agreement with experimental measurements, generally, $\langle\bar{u}''^2\rangle^{1/2} > \langle\bar{w}^2\rangle^{1/2} > \langle\bar{v}^2\rangle^{1/2}$ throughout the channel. In addition, $\langle\bar{u}''^2\rangle^{1/2}$ and $\langle\bar{w}^2\rangle^{1/2}$ attain their maximum values near the wall. Figure 19 shows the profile of the resolvable turbulent shear stress, $\langle\bar{u}\bar{v}\rangle$. It can be seen that in the regions away from the walls the profile of $\langle\bar{u}\bar{v}\rangle$ does not follow the theoretical line. This indicates that the statistically stationary state has not been reached completely. Note that near the wall viscous stresses are important, and the total shear stress must balance the gross pressure gradient. Moreover, in the present calculations, the subgrid-scale shear stresses are significant only very near the wall ($y^+ < 10$). In Fig. 20, profiles of the intensities are compared with some of the available experimental data in the vicinity of the wall. The agreement of the computed $\langle\bar{u}''^2\rangle^{1/2}$ and $\langle\bar{w}^2\rangle^{1/2}$ with the data is satisfactory. However, as was also the case in Ref. 9, near the wall, a significant portion of $\langle\bar{v}^2\rangle^{1/2}$ seems to reside in subgrid-scale motions. This is consistent with our previous observation that ν_T is still excessively large near the walls.

Figure 21 shows the resolvable portions of the pressure velocity-gradient correlations, $\langle\bar{p}(\partial\bar{u}/\partial x)\rangle$, $\langle\bar{p}(\partial\bar{v}/\partial y)\rangle$, and $\langle\bar{p}(\partial\bar{w}/\partial z)\rangle$ in the vicinity of the wall ($y^+ < 100$, t = 2.0). These terms are responsible for the exchange of energy between the three components of resolvable turbulence kinetic energy; they are of particular interest to turbulence modelers. Examination of these profiles reveals that except in the immediate neighborhood of the wall ($y^+ < 20$), as expected, energy is transferred from $\langle\bar{u}''^2\rangle$ to $\langle\bar{v}^2\rangle$ and $\langle\bar{w}^2\rangle$; that is, $\langle\bar{p}(\partial\bar{u}/\partial x)\rangle < 0$, and $\langle\bar{p}(\partial\bar{v}/\partial y)\rangle$, $\langle\bar{p}(\partial\bar{w}/\partial z)\rangle > 0$. On the other hand, as we approach the wall, a significantly different behavior can be noticed. Specifically, there is a relatively large rate of energy transfer from $\langle\bar{v}^2\rangle$, whereas there is a large energy transfer to $\langle\bar{w}^2\rangle$. This rather unexpected result is consistent nonetheless with our previous discussions of the fluid motions very close to the wall (Sec. 7). For example, Fig. 15a shows high-speed fluid approaching the wall and spreading laterally, resulting in relatively large energy transfer from $\langle\bar{v}^2\rangle$ to $\langle\bar{w}^2\rangle$. On the other hand, the momentum transfer from the lateral to the normal directions, which results in ejection of fluid elements away from the wall, involves the nonenergetic (slow moving) fluid in the immediate neighborhood of the wall. Thus, there is a net energy transfer from $\langle\bar{v}^2\rangle$ to $\langle\bar{w}^2\rangle$, as shown in Fig. 21.

It should be mentioned that, in general, the values of the pressure velocity-gradient correlations computed in the present study are significantly higher than the earlier results using a much coarser grid (Ref. 9). This may indicate that a substantial portion of the pressure-strain correlation is due to small-to-medium turbulence scales. To confirm this observation, several computations were carried out with different filter widths. The results of the calculations tend to support this observation. Thus, at present, and in the absence of a better subgrid-scale turbulence theory, the computed pressure-strain correlations should be interpreted qualitatively. It should be mentioned, however, that the large-scale flow structures presented in the previous section are rather insensitive (qualitatively) to the different filter widths and subgrid-scale models used.

Before concluding this section, we turn our attention again to the subgrid-scale model used in the present study. To better resolve the relatively small turbulence scales in the vicinity of the walls, the present calculations were carried out for the case of a relatively low Reynolds number turbulent channel flow (Re_τ = 640, Re = 13,800). Therefore, the subgrid-scale turbulence Reynolds number defined in Sec. 3 is considered to be low in the regions away from the wall and very low in the vicinity of the walls. As was mentioned in Sec. 3, the arguments used in constructing this model are valid only at a very high Reynolds number. Numerical results of McMillan and Ferziger (Ref. 30) also show that Smagorinsky's model is more appropriate at high Reynolds numbers. Thus, a low Reynolds number correction seems to be necessary. Note that because of the use of a much finer grid in this simulation than that used in Ref. 9, the effective subgrid-scale turbulence Reynolds number is lower than that in Ref. 9. In addition, because of the quasi-cyclic nature of turbulent channel flow (bursts, sweeps, etc.) the present calculations seem to indicate that a subgrid-scale model that has a better response to the time history of the flow (a dynamic model) than the simple eddy viscosity model used here may be necessary. This is necessary for a proper long-time integration of the governing equations. Integrating an additional equation for subgrid-scale turbulence energy is an attractive possibility. In the interim, however, we have found that selective filtering of the excess small-scale turbulence may be adequate.

9. CONCLUSIONS

In this study, the three-dimensional time-dependent equations of motion have been numerically integrated for the case of fully-developed turbulent channel flow. The calculations were carried out on the ILLIAC IV computer with 64 mesh points in each of the spatial directions. Detailed flow patterns were studied by examining contour plots of typical instantaneous velocity and vorticity fields. In summary:

1. The wall layer consisted of coherent structures of low-speed and high-speed streaks alternating in the spanwise direction. These structures are absent in the regions away from the wall. In addition, contour plots of velocities in a typical y-z plane revealed the existence of well-organized flow patterns in the wall region.

2. Hot spots, small localized regions of very large values of turbulent shear stress, $\bar{u}''\bar{v}$, were frequently observed. Very close to the wall, these hot spots were associated with $\bar{u}'' > 0$ and $\bar{v} < 0$ (sweep); away from the wall, they were due to $\bar{u}'' < 0$ and $\bar{v} > 0$ (burst). In the central regions of the channel, bursts from both halves of the channel were the sources of the hot spots.

3. No evidence of a direct relationship between streaks and streamwise vorticity $\bar{\omega}_x$ was observed in the present simulation; very close to the wall, $\bar{\omega}_x$ was not the result of large-scale revolving fluid motions but was rather due to the spanwise velocity gradient, $(\partial\bar{w}/\partial y)$. Though strong vortical regions were observed away from the wall ($y^+ \sim 30$), $\langle\bar{\omega}_x^2\rangle^{1/2}$ attained its maximum value at the wall.

4. The profiles of the pressure velocity-gradient correlation showed a significant transfer of energy from the normal to the spanwise component of turbulent kinetic energy in the immediate neighborhood of the wall (the "splatting" effect). A large portion of the pressure-strain correlations appears to be due to small to medium scales of turbulent motions.

The work presented here is still in progress and much more remains to be done. In particular, a more refined model that depicts the dynamic nature of the subgrid-scale motion may become necessary. Also, more mesh points, especially in the spanwise direction, are required in order to resolve the streaks at their proper scale. A computation with twice as many grid points as in the present calculation (64 × 64 × 128) will be carried out in the near future.

It is hoped that this paper has demonstrated some of the capabilities of LES as a research tool for studying the mechanics and structure of turbulent boundary layers. The authors believe that LES will make important contributions to the study of turbulent flows by supplementing the experimental data.

REFERENCES

1. Chapman, D. R.: Computational Aerodynamics Development and Outlook. AIAA Dryden Lectureship in Research. AIAA Paper 79-0129, January 1979.

2. Kwak, D., Reynolds, W. C., and Ferziger, J. H.: Three-Dimensional, Time-Dependent Computation of Turbulent Flows. Report No. TF-5, Mech. Eng. Dept., Stanford Univ., 1975.

3. Shaanan, S., Ferziger, J. H., and Reynolds, W. C.: Numerical Simulation of Turbulence in the Presence of Shears. Report No. TF-6, Mech. Eng. Dept., Stanford Univ., 1975.

4. Mansour, N. N., Moin, P., Reynolds, W. C., and Ferziger, J. H.: Improved Methods for Large Eddy Simulation of Turbulence. Proc. Symp. on Turbulent Shear Flows, Pennsylvania State Univ., 1977.

5. Deardorff, J. W.: A Numerical Study of Three-Dimensional Turbulent Channel Flow at Large Reynolds Number. J. Fluid Mech., vol. 41, 1970, p. 283.

6. Schumann, U.: Subgrid Scale Model for Finite Difference Simulations of Turbulent Flows in Plane Channels and Annuli. J. Comp. Phys., vol. 18, 1975, p. 376.

7. Kim, H. T., Kline, S. J., and Reynolds, W. C.: The Production of Turbulence Near a Smooth Wall in a Turbulent Boundary Layer. J. Fluid Mech., vol. 50, 1971, p. 133.

8. Rajagopalan, S., and Antonia, R. A.: Some Properties of the Large Structure in a Fully Developed Turbulent Duct Flow. Phys. Fluids, vol. 22, 1979, p. 614.

9. Moin, P., Reynolds, W. C., and Ferziger, J. H.: Large Eddy Simulation of Incompressible Channel Flow. Report No. TF-12, Mech. Eng. Dept., Stanford Univ., 1978.

10. Leonard, A.: On the Energy Cascade in Large-Eddy Simulations of Turbulent Fluid Flows. Adv. In Geophysics, vol. 18A, 1974, p. 237.

11. Lilly, D. K.: The Representation of Small-Scale Turbulence in Numerical Simulation Experiments. Proc. IBM Sci. Comp. Symp. on Env. Sciences, IBM Form No. 320-1951, 1967.

12. Ferziger, J. H., Mehta, U. B., and Reynolds, W. C.: Large Eddy Simulation of Homogeneous Isotropic Turbulence. Proc. Symp. on Turbulent Shear Flows, Pennsylvania State Univ., 1977.

13. Comte-Bellot, G.: Contribution a l'etude de la Turbulenc' de Conduite, Doctoral Thesis, University of Grenoble, 1963.

14. Kline, S. J., Reynolds, W. C., Schraub, F. A., and Runstadler, P. W.: The Structure of Turbulent Boundary Layers. J. Fluid Mech., vol. 30, 1967, p. 741.

15. Moin, P., Mansour, N. N., Reynolds, W. C., and Ferziger, J. H.: Large Eddy Simulation of Turbulent Shear Flows. Proc. Sixth International Conference on Numerical Methods in Fluid Dynamics, Cabannes, H., Holt, M., and Rusanov, V., eds., Springer-Verlag, Berlin, Heidelberg, New York, 1979.

16. Orszag, S. A.: Comparison of Pseudospectral and Spectral Approximation. Studies in Appl. Math., vol. LI, no. 3, 1972, p. 253.

17. Lilly, D. K.: On the Computational Stability of Numerical Solutions of Time-Dependent Nonlinear Geophysical Fluid Dynamic Problems. Monthly Weather Rev., vol. 93, no. 1, 1965.

18. Richtmyer, R. D., and Morton, K. W.: Difference Methods for Initial Value Problems, Second ed. Interscience, New York, 1967.

19. Rogallo, R. S.: An ILLIAC Program for the Numerical Simulation of Homogeneous Incompressible Turbulence. NASA TM-73203, 1977.

20. Runstadler, P. W., Kline, S. J., and Reynolds, W. C.: An Investigation of the Flow Structure of the Turbulent Boundary Layer. Report No. MD-8, Mech. Eng. Dept., Stanford Univ., 1963.

21. Kline, S. J., and Runstadler, P. W.: Some Preliminary Results of Visual Studies of Wall Layers of the Turbulent Boundary Layer. J. Appl. Mech., vol. 2, 1959, p. 166.

22. Falco, R. E.: The Role of Outer Flow Coherent Motions in the Production of Turbulence Near a Wall. Coherent Structure of Turbulent Boundary Layers, Smith, C. R., and Abbott, D. E., eds., AFOSR/Lehigh, 1978.

23. Brodkey, R. S., Wallace, J. M., and Eckelmann, H.: Some Properties of Truncated Turbulence Signals in Bounded Shear Flows. J. Fluid Mech., vol. 63, 1974, p. 209.

24. Sabot, J. and Comte-Bellot, G.: Intermittency of Coherent Structures in the Core Region of Fully Developed Turbulent Pipe Flow. J. Fluid Mech., vol. 74, 1976, p. 767.

25. Blackwelder, R. F.: The Bursting Process in Turbulent Boundary Layers. Coherent Structure of Turbulent Boundary Layers, C. R. Smith and D. E. Abbott, eds., AFOSR/Lehigh, 1978.

26. Fornberg, B.: A Numerical Study of 2-D Turbulence. J. Comp. Phys., vol. 25, 1977, p. 1.

27. Hussain, A. K. M. F. and Reynolds, W. C.: Measurements in Fully Developed Channel Flow. J. Fluid Eng., vol. 97, 1975, p. 568.

28. Laufer, J.: Investigation of Turbulent Flow in a Two-Dimensional Channel. NACA Report 1053, 1951.

29. Clark, J. A.: A Study of Incompressible Turbulent Boundary Layers in Channel Flow. J. Basic Engrg., vol. 90, 1968, p. 455.

30. McMillan, O. J. and Ferziger, J. H.: Direct Testing of Subgrid-Scale Models, NEAR TR 174. Nielsen Engineering and Research, Inc., 1978.

ACKNOWLEDGMENT

This work was carried out while the authors held NRC Research Associateships at Ames Research Center. The authors would like to express their gratitude to Dr. R. S. Rogallo for his assistance in writing the present program for the ILLIAC IV computer. Helpful discussions with Drs. A. Leonard, M. W. Rubesin, and A. W. Wray are gratefully acknowledged.

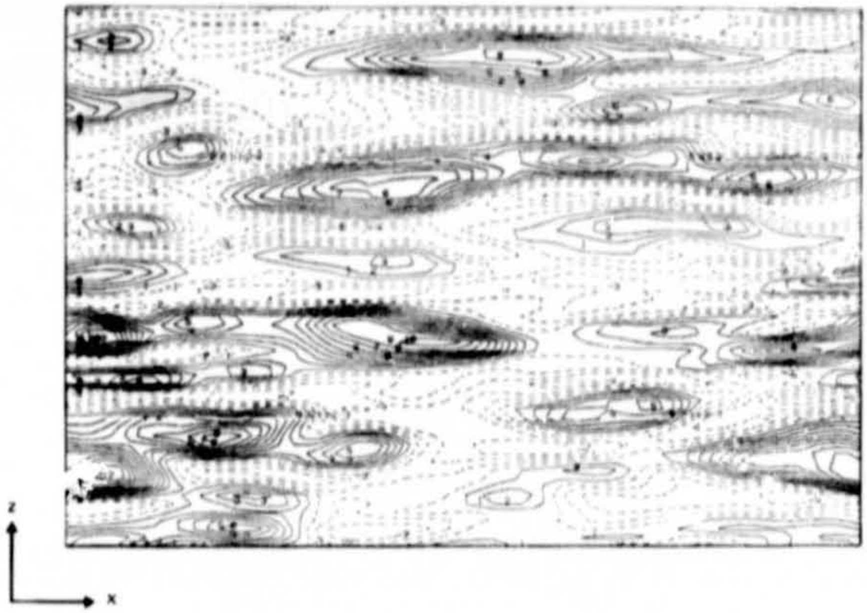

Fig. 1. Contours of $\tilde{u}''$ in the x-z plane at $y^+ = 16$.

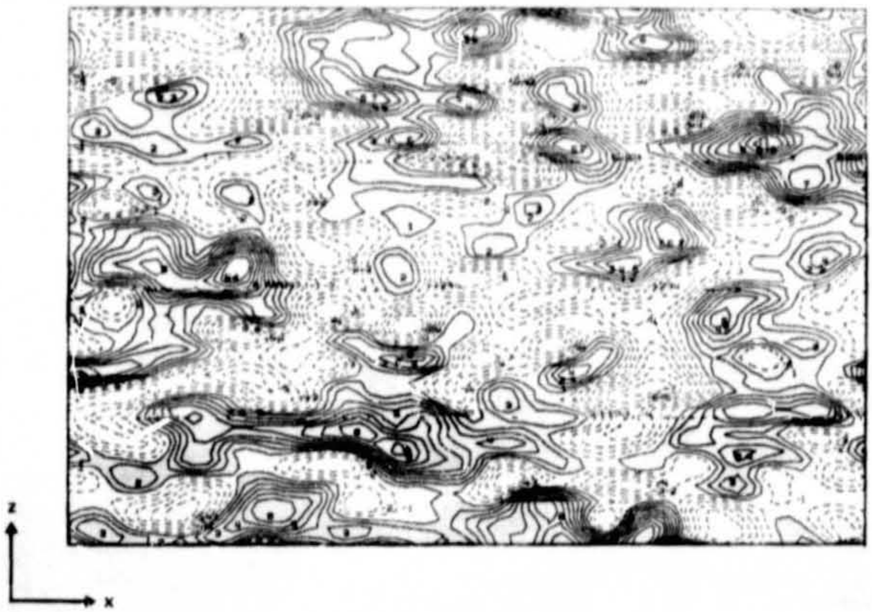

Fig. 2. Contours of $\tilde{u}''$ in the x-z plane at $y/\delta = 0.73$.

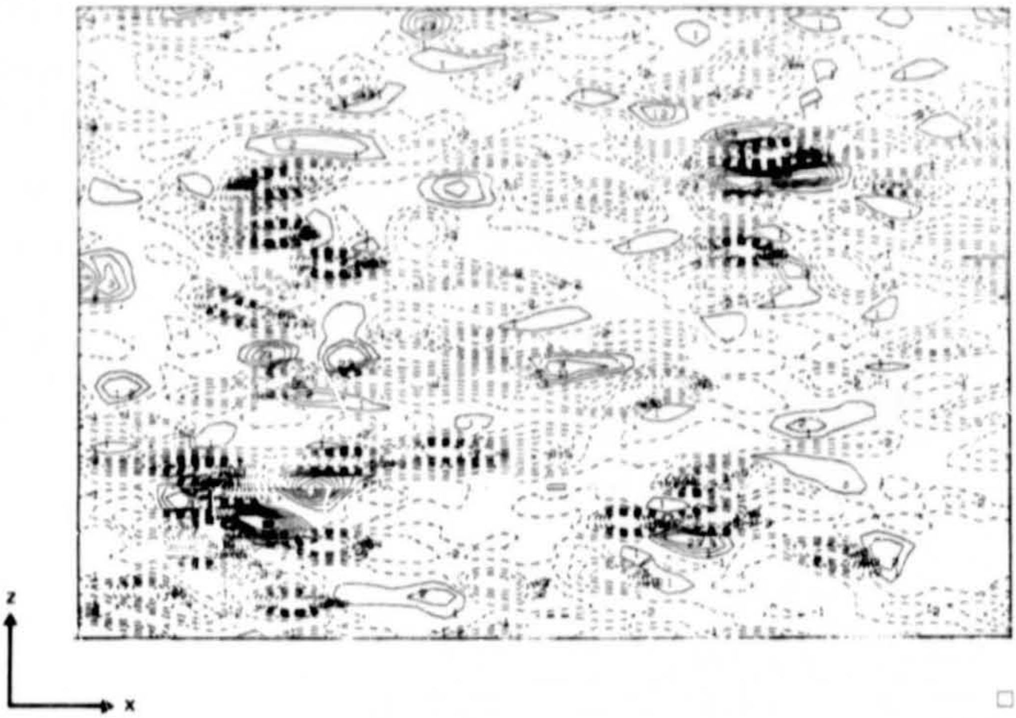

Fig. 3. Contour plot of $\tilde{u}''\tilde{v}$ in the x-z plane at $y^+ = 16$.

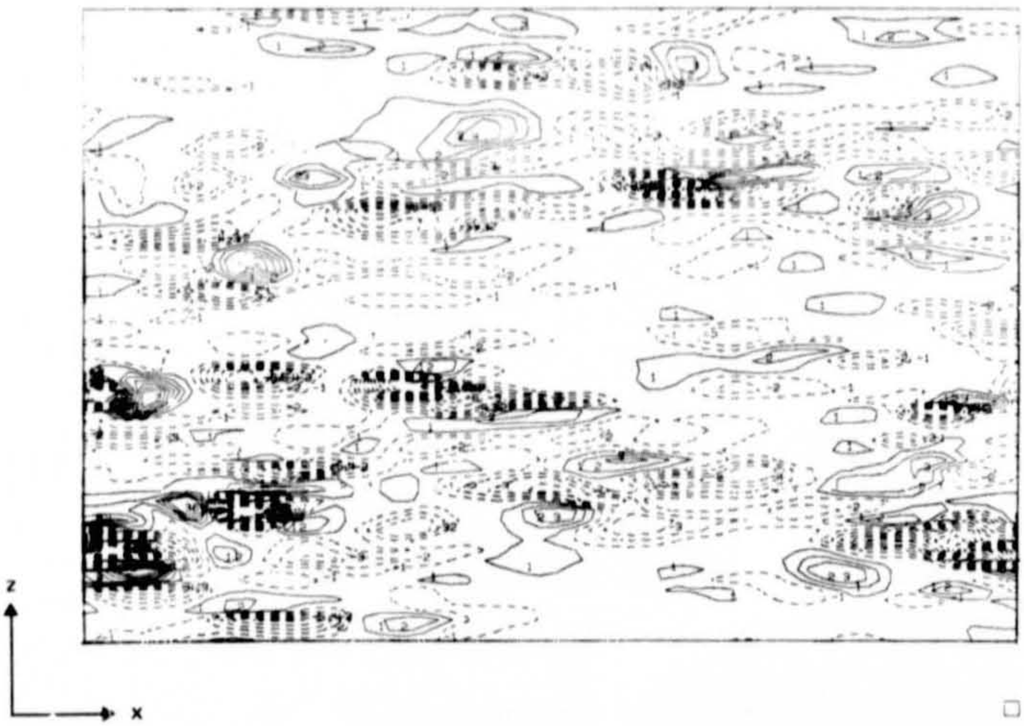

Fig. 4. Contour plot of $\tilde{u}''\tilde{v}$ in the x-z plane at $y^+ = 90$.

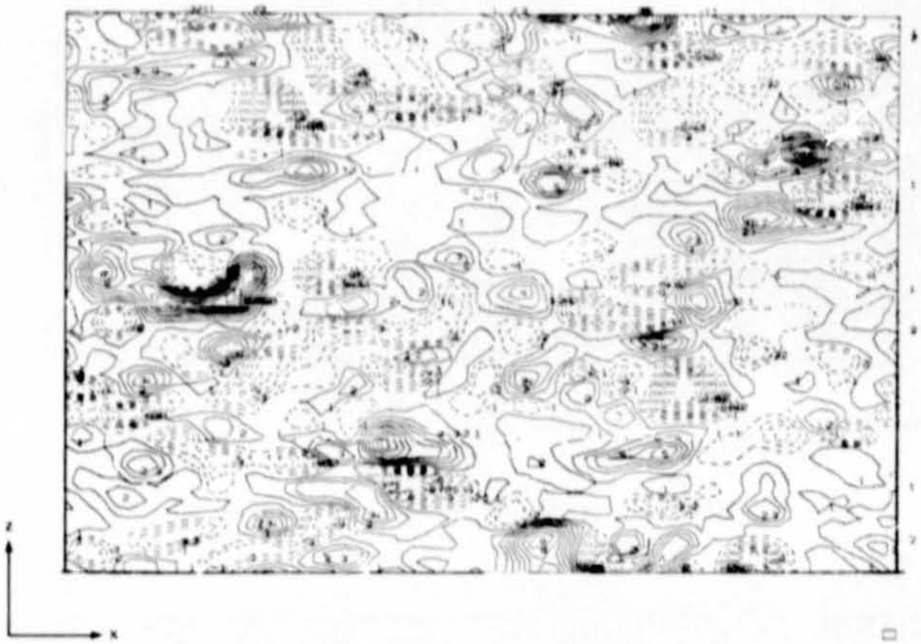

Fig. 5. Contour plot of $\tilde{u}''\tilde{v}$ in the x-z plane at $y/\delta = 0.73$.

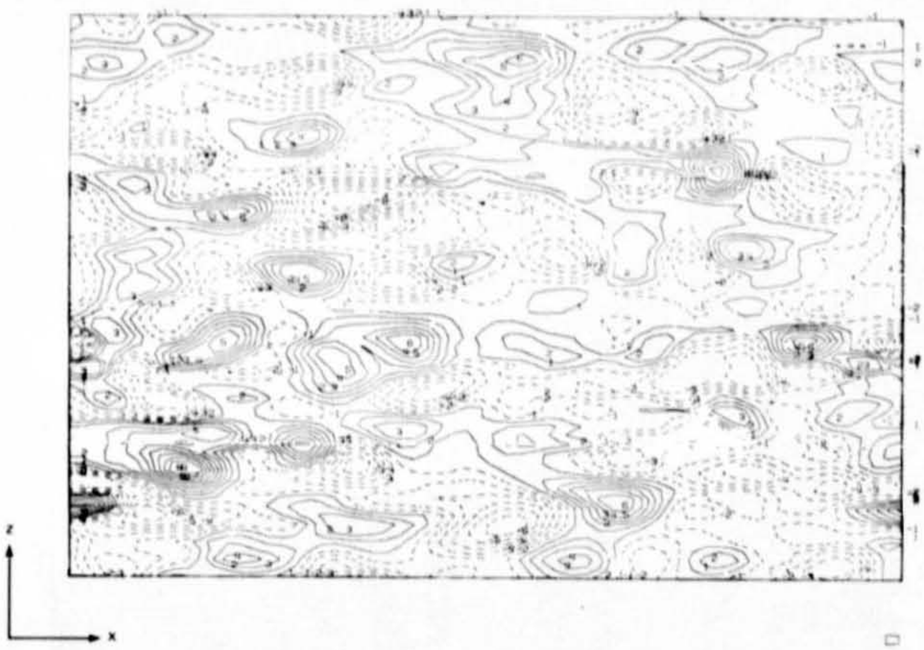

Fig. 6. Contours of the streamwise vorticity $\tilde{\omega}_x$ in the x-z plane at $y^+ = 16$. Note that the $\tilde{\omega}_x$ patterns do not exhibit elongated structures in the x-direction.

Fig. 7. Contours of $\tilde{u}''$ in the x-y plane ($0 \leq y/\delta \leq 0.5$) at $z = 15h_3$.

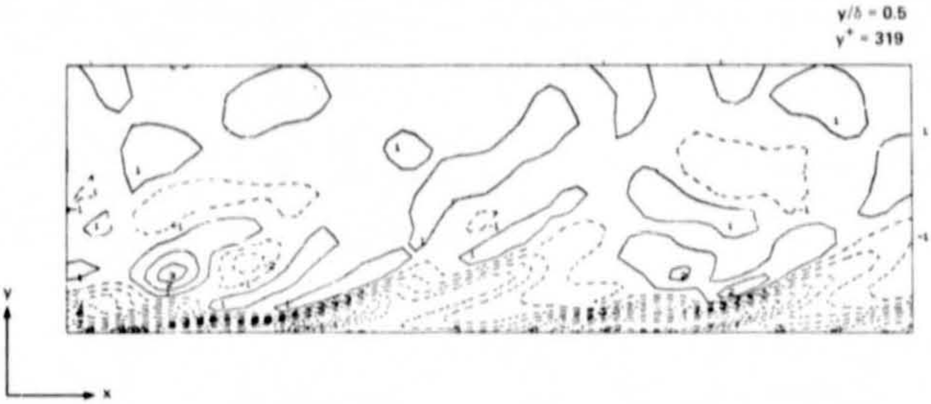

Fig. 8. Contours of spanwise vorticity $\tilde{\omega}_z$ in the x-y ($0 \leq y/\delta \leq 0.5$) plane at $z = 15h_3$.

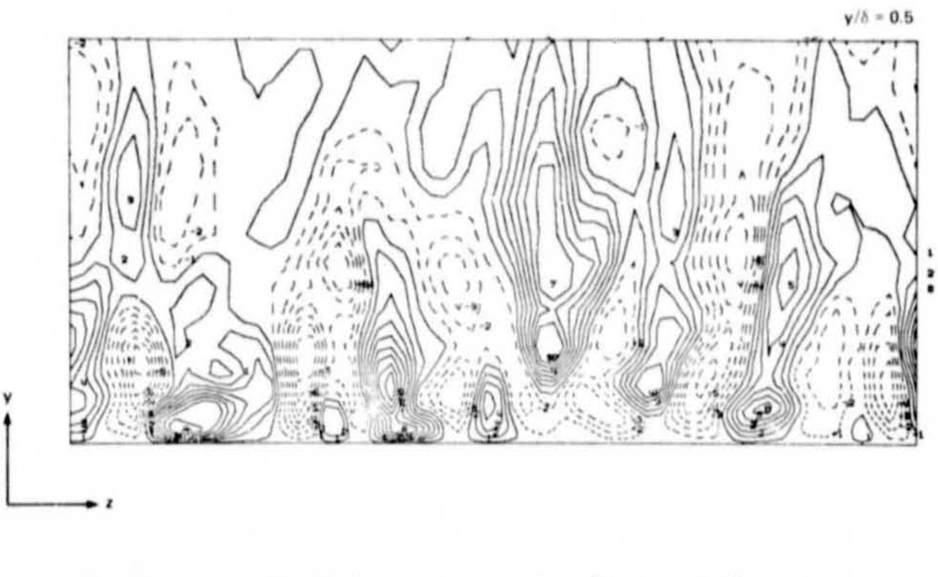

Fig. 9. Contour plot of $\tilde{u}''$ in the y-z plane ($0 \leq y/\delta \leq 0.5$) at $x = 0$.

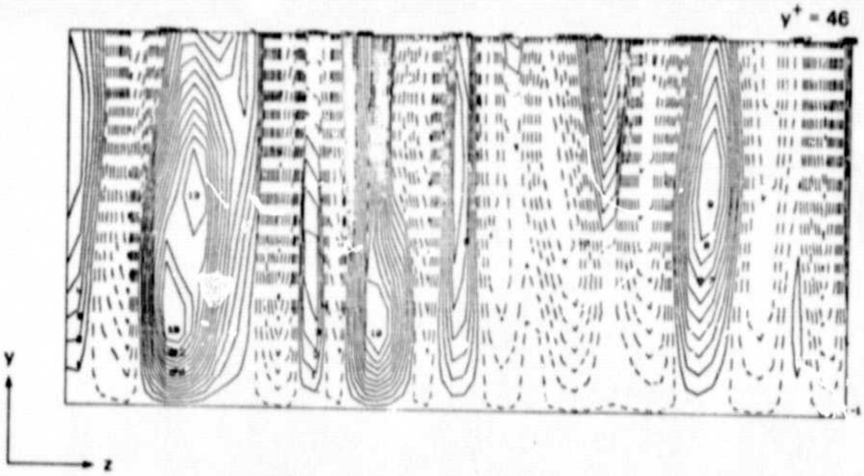

Fig. 10. Contour plot of $\tilde{u}''$ in the y-z plane $(0 \leq y^+ \leq 46)$ at $x = 0$.

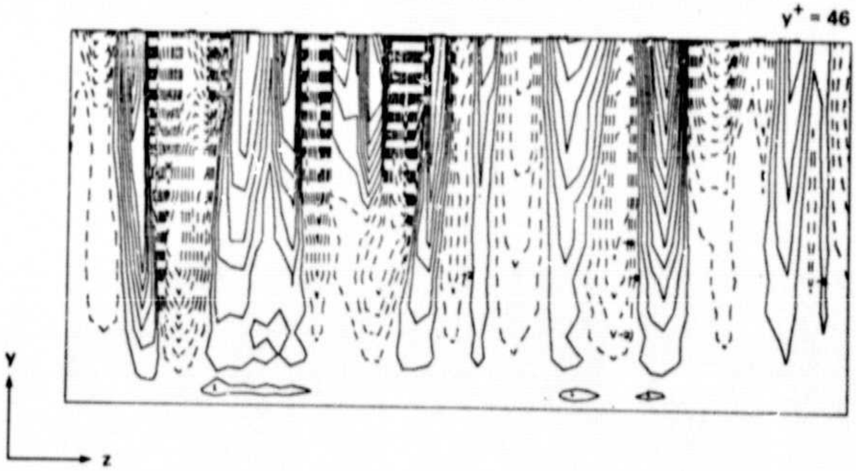

Fig. 11. Contour plot of $\tilde{v}$ in the y-z plane $(0 \leq y^+ \leq 46)$ at $x = 0$.

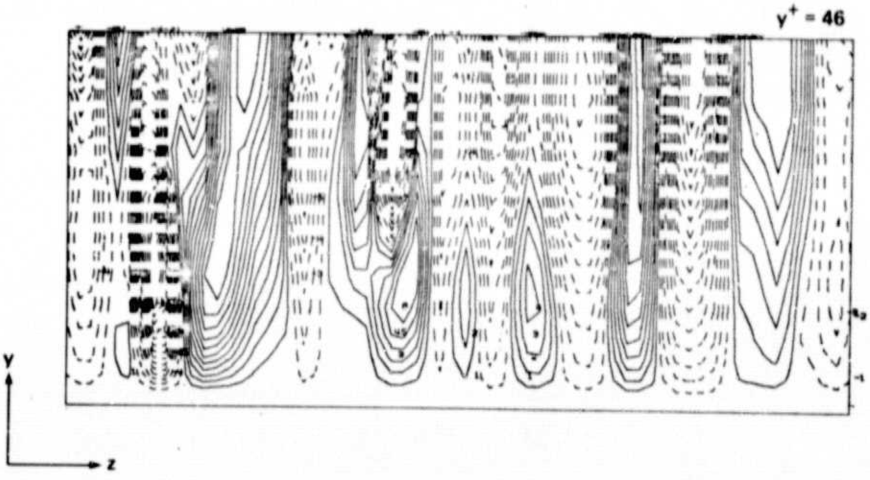

Fig. 12. Contours of $\tilde{w}$ in the y-z plane $(0 \leq y^+ \leq 46)$ at $x = 0$.

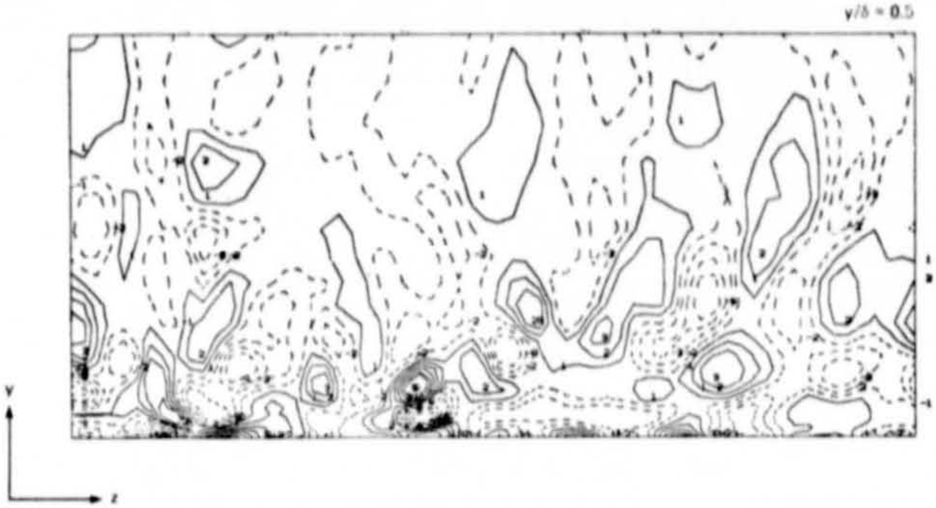

Fig. 13. Contour plot of the streamwise vorticity in the y-z plane ($0 \leq y/\delta \leq 0.5$) at $x = 0$.

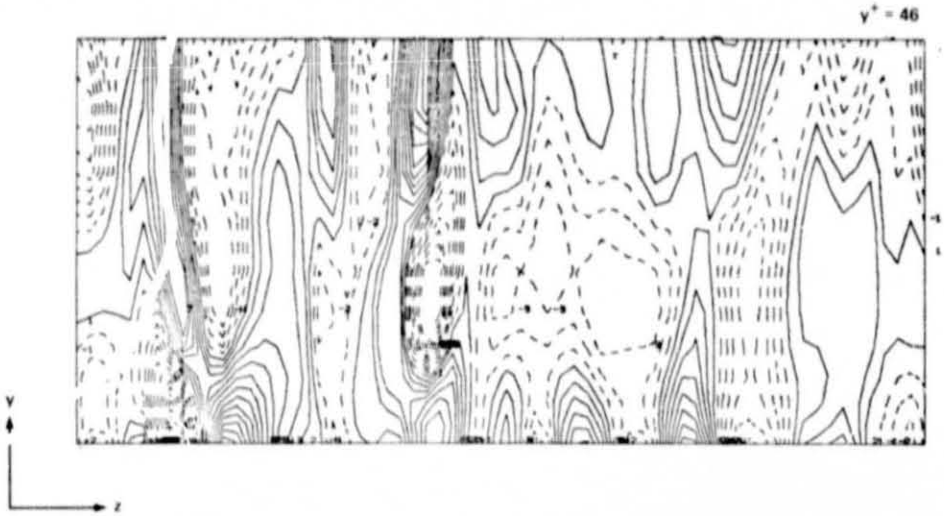

Fig. 14. Contours of the streamwise vorticity in the y-z plane ($0 \leq y^+ \leq 46$) at $x = 0$.

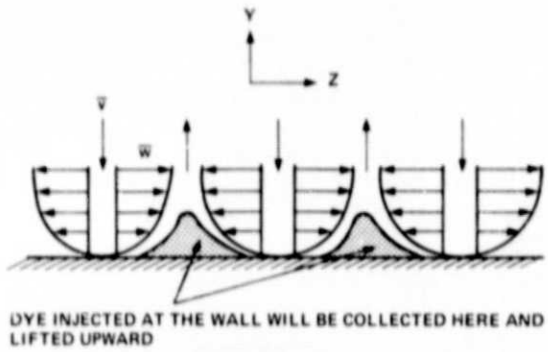

(a) Cross-sectional view of spanwise velocity in y-z plane.

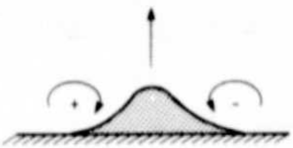

(b) Streamwise vorticity according to (a).

Fig. 15. Schematic diagram of the flow patterns in the immediate neighborhood of the wall.

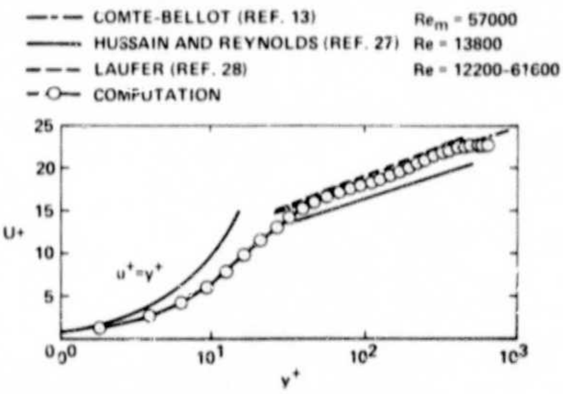

Fig. 16. Mean-velocity profile.

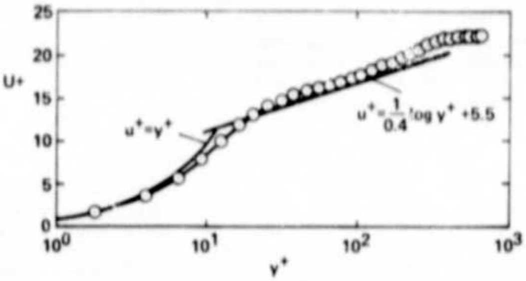

Fig. 17. Mean-velocity profile obtained with the sharp cutoff model (Ref. 26).

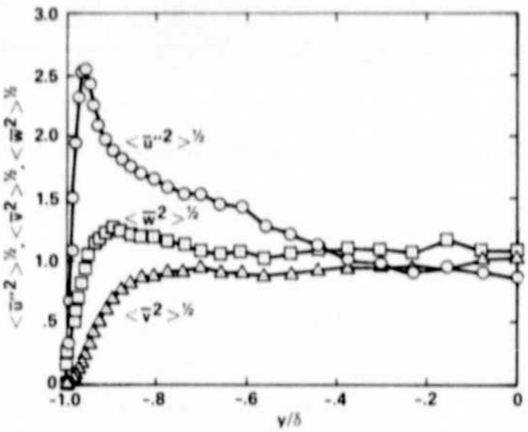

Fig. 18. Profiles of horizontally averaged resolvable turbulence intensities.

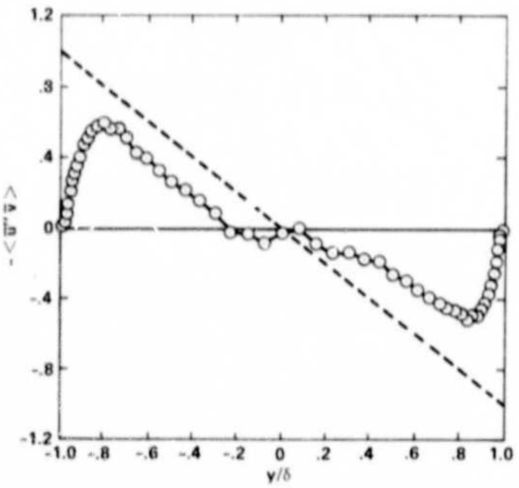

Fig. 19. Vertical profile of horizontally averaged resolvable turbulent shear stress.

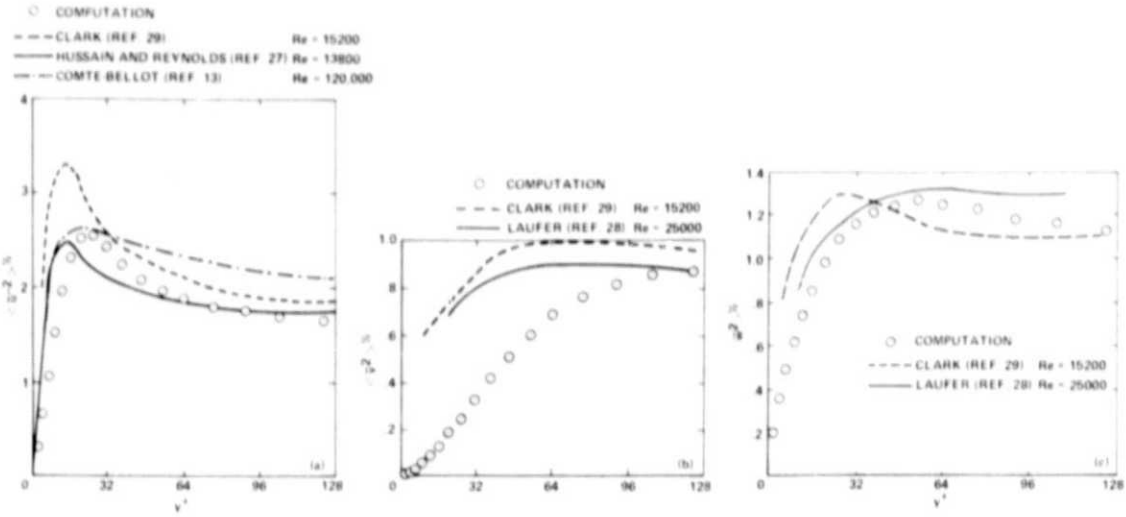

Fig. 20. Comparison of the horizontally averaged resolvable turbulence intensities with experimental data.

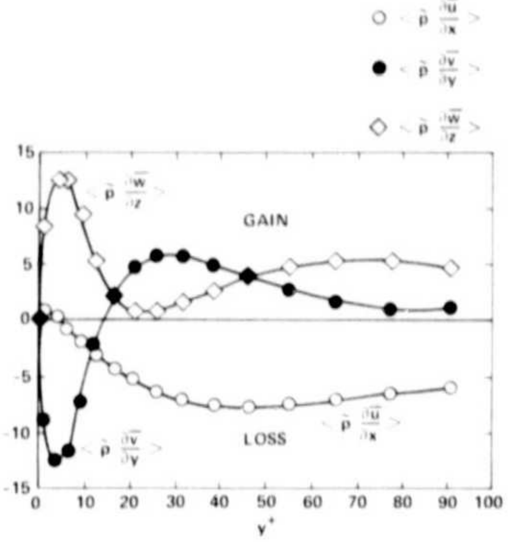

Fig. 21. Vertical profiles of horizontally averaged resolvable pressure velocity gradient correlations in the vicinity of the wall ($y^+ \leq 100$).